

The Latent Color Subspace: Emergent Order in High-Dimensional Chaos

Mateusz Pach^{*123} Jessica Bader^{*123} Quentin Bouniot¹²³ Serge Belongie⁴ Zeynep Akata¹²³

Abstract

Text-to-image generation models have advanced rapidly, yet achieving fine-grained control over generated images remains difficult, largely due to limited understanding of how semantic information is encoded. We develop an interpretation of the color representation in the Variational Autoencoder latent space of FLUX.1 [Dev], revealing a structure reflecting Hue, Saturation, and Lightness. We verify our Latent Color Subspace (LCS) interpretation by demonstrating that it can both predict and explicitly control color, introducing a fully training-free method in FLUX based solely on closed-form latent-space manipulation. Code is available at <https://github.com/ExplainableML/LCS>.

1. Introduction

Flow Matching (FM) models are increasingly capable of generating high-quality, accurate images, enabling their use across a wide range of practical applications (Dinkevich et al., 2025; Yellapragada et al., 2024; Wang et al., 2025). Nonetheless, precise and reliable control over generated images remains a significant challenge, despite being essential for many of these applications. Prior work improved controllability for image generation (Zhang et al., 2023a; Ye et al., 2023) and editing (Labs et al., 2025). However, these approaches often depend on additional models or training, increasing system complexity without substantially improving understanding of the underlying mechanisms. This lack of insight makes it difficult to establish trust in the system. Rather than increasing system complexity, we aim to develop a clearer interpretation of how FLUX.1 [Dev] (FLUX) (BlackForest, 2024) processes a fundamental image component: color. To validate our interpretation, we want to show two key properties: it is (1) *accurate*, faithfully reflecting the final image’s emerging features, and (2) *causal*,

^{*}Equal contribution ¹Technical University of Munich ²Helmholtz Munich ³Munich Center for Machine Learning ⁴University of Copenhagen. Correspondence to: Mateusz Pach <mateusz.pach@tum.de>.

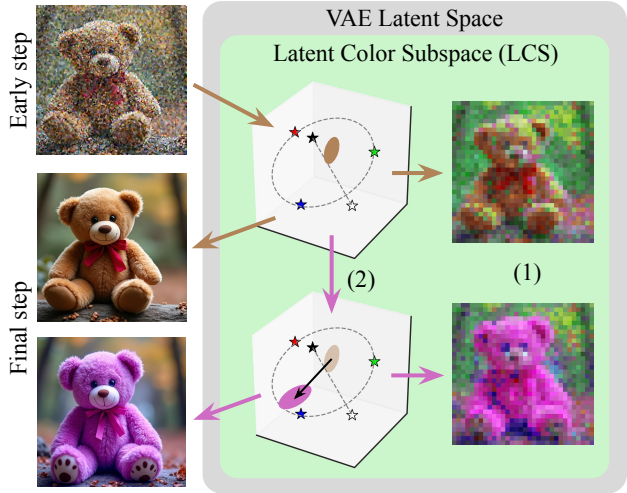


Figure 1. We find a simple color subspace in the VAE embedding space of FLUX which can be interpreted as cylindrical coordinates corresponding to Hue, Saturation, and Lightness, enabling (1) inexpensive observation and (2) targeted intervention.

enabling deliberate intervention. Unfortunately, achieving such understanding in text-to-image (T2I) generation models is difficult due to deep learning’s black-box nature, a challenge further compounded by the step-wise prediction process of T2I generation and its operation within the high-dimensional latent space of a variational autoencoder (VAE), which is itself largely uninterpretable.

Still, we develop and verify a simple interpretation of color in the VAE latent space of FLUX (BlackForest, 2024). We observe that color occupies a three-dimensional subspace, forming a bicone-like structure that closely mirrors the Hue–Saturation–Lightness (HSL) representation. By combining this insight with an understanding of how image patches evolve across FM timesteps, we construct a functional interpretation of color in the latent space that generalizes across HSL colors. This allows color to be interpreted at intermediate timesteps directly in the latent space through lightweight transformations, without needing the 50-million-parameter VAE decoder. We validate the accuracy of our interpretation by using it to *observe* mid-generation color representations in the latent space and *intervene*, guiding the generation toward target colors. When combined with se-

semantic segmentation, this intervention enables fine-grained control over the colors of specific objects (see Figure 1).

The primary contributions of this work are threefold: (1) To our knowledge, we are the first to show that color lives in a three-dimensional subspace of FLUX’s VAE latent space, closely resembling HSL representation; (2) We leverage this understanding to develop a working interpretation of color encoding that generalizes across the full HSL color space; (3) We introduce a novel, entirely training-free localized color-intervention method that relies solely on a mechanistic understanding of FLUX’s internal representations.

2. Related Works

The adoption of diffusion models (Rombach et al., 2022) has transformed T2I generation, typically operating in the latent space of a VAE (Kingma & Welling, 2014). These models have improved in image quality and prompt adherence (OpenAI, 2023; Midjourney, 2025; DeepMind, 2025; Podell et al., 2023; Chen et al., 2024), recently shifting toward transformer-based diffusion architectures (Peebles & Xie, 2023; Esser et al., 2024; BlackForest, 2024; Wu et al., 2025) and taking on a FM perspective (Lipman et al., 2022; Albergo & Vanden-Eijnden, 2023; Liu et al., 2023). Despite these advances, fine-grained control remains limited across several dimensions, including pose and layout (Zhang et al., 2023b), spatial positioning (Bader et al., 2025b), and color (Mantecon et al., 2026). These limitations have motivated work on controllable generation through optimization (Zhang et al., 2023b; Eyring et al., 2024; 2025; Li et al., 2023; Farshad et al., 2023; Shum et al., 2025b), though training-free approaches have also been explored (Bader et al., 2025a;b; Oorloff et al., 2025).

Despite rapid advances in T2I models, their underlying mechanisms remain less explored. Prior work has begun to uncover key internal processes, including why they generalize (Niedoba et al., 2025), how they generate spatial relations (Wang et al., 2026), and how biases emerge (Shi et al., 2025). Complementary approaches leverage attention mechanisms within T2I models to analyze or control generation (Chefer et al., 2023; Hertz et al., 2023; Tang et al., 2023), as well as sparse autoencoders to identify interpretable and intervenable directions in model representations (Kim et al., 2025b; Daujotas, 2024; Shabalin et al., 2025; Shi et al., 2025). Furthermore, attention mechanisms in DiT models have proven effective for segmentation (Kim et al., 2025a; Helbling et al., 2025; Hu et al., 2025).

Color control in FM models has been studied via color conditioning (Shum et al., 2025a) and color–style disentanglement (Zhang et al., 2025). It can be enabled by learned color prompts (Butt et al., 2024), IP-Adapters (Mantecon et al., 2026), and inpainting or ControlNet-based approaches (Liu

et al., 2025). These methods increase model complexity without improving interpretability, whereas ours leverages understanding to enable control. Others focus on color control in editing (Liang et al., 2025; Vavilala et al., 2025; Yang et al., 2025). Concurrent work analyzes color encoding in the VAE latent space (Arias et al., 2025) but is more limited, lacking prediction, intervention, and temporal FM analysis.

3. Analysis of Color in FM VAE Space

To develop an interpretation of color in FLUX, we must understand how color is represented in the VAE space and how this space is traversed during the denoising process.

3.1. Preliminaries

Variational Autoencoder Modern FM models operate in a compressed embedding. FLUX and many others use a VAE’s latent space for this purpose. Given input image \mathbf{x} , the VAE encoder produces parameters $\boldsymbol{\mu}(\mathbf{x})$ and $\boldsymbol{\sigma}(\mathbf{x})$ of a diagonal Gaussian posterior distribution

$$q_{\phi}(\mathbf{z} | \mathbf{x}) = \mathcal{N}(\mathbf{z}; \boldsymbol{\mu}(\mathbf{x}), \text{diag}(\boldsymbol{\sigma}(\mathbf{x})^2)).$$

A latent sample is obtained with the reparameterization trick

$$\mathbf{z} = \boldsymbol{\mu}(\mathbf{x}) + \boldsymbol{\sigma}(\mathbf{x}) \odot \boldsymbol{\epsilon}, \quad \boldsymbol{\epsilon} \sim \mathcal{N}(\mathbf{0}, \mathbf{I}).$$

The VAE decoder reconstructs the image as

$$\hat{\mathbf{x}} = p_{\theta}(\mathbf{x} | \mathbf{z}).$$

Training minimizes the evidence lower bound (ELBO),

$$\mathcal{L}_{\text{VAE}} = \mathbb{E}_{q_{\phi}(\mathbf{z}|\mathbf{x})} [\mathcal{L}_{\text{rec}}(\mathbf{x}, \hat{\mathbf{x}})] + \beta D_{\text{KL}}(q_{\phi}(\mathbf{z} | \mathbf{x}) \| \mathcal{N}(\mathbf{0}, \mathbf{I})),$$

which balances reconstruction fidelity with regularization of the latent distribution toward a unit Gaussian prior.

Flow Matching FLUX is trained with FM objective. Let $\mathbf{z}_0 \sim \mathcal{N}(\mathbf{0}, \mathbf{I})$ denote an initial noise sample in latent space and \mathbf{z}_1 a clean latent encoding of an image obtained from the VAE. FM learns a continuous-time velocity field $\mathbf{v}_{\theta}(\mathbf{z}, t)$ that transports samples from the noise distribution to the data distribution by minimizing

$$\mathcal{L}_{\text{FM}} = \mathbb{E}_{t \sim \mathcal{U}(0,1), \mathbf{z}_t} \left[\left\| \mathbf{v}_{\theta}(\mathbf{z}_t, t) - \frac{d\mathbf{z}_t}{dt} \right\|^2 \right],$$

where the interpolation path is defined as

$$\mathbf{z}_t = (1 - t) \mathbf{z}_0 + t \mathbf{z}_1, \quad \frac{d\mathbf{z}_t}{dt} = \mathbf{z}_1 - \mathbf{z}_0.$$

In practice, the model predicts the velocity $\mathbf{z}_1 - \mathbf{z}_0$ from an interpolated latent \mathbf{z}_t and timestep t , conditioned on text embeddings. At inference, the learned velocity field is integrated with a numerical solver (Euler discretization in our case) to transport pure noise to a clean latent sample.

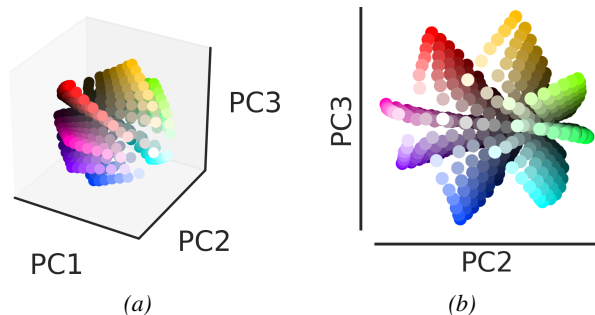


Figure 2. PCA shows color organization in the VAE latent space mirrors HSL: Hue forms a circle on the PC2–PC3 plane, Saturation is distance from the black-white axis, and Lightness lies on PC1.

3.2. Color Representation in the VAE Space

To explore VAE-space color representation, we use $N = 512$ solid-color images, sampled uniformly from Hue–Saturation–Value (HSV) space. Each image n is encoded with FLUX’s VAE encoder, producing latents $\mathbf{Z}^n \in \mathbb{R}^{L \times d}$, where L is the number of patches and d is patch dimensionality. We average each image’s L patches, obtaining a single latent vector $\bar{\mathbf{z}}^n \in \mathbb{R}^d$. Applying PCA to these N latent vectors, after centering by their mean $\boldsymbol{\mu} \in \mathbb{R}^d$, reveals that the first three principal components (PC) $\mathbf{B} \in \mathbb{R}^{d \times 3}$ account for 100% of the variance, indicating that color information is confined to a 3D subspace of the VAE latent space. We refer to this subspace as the **Latent Color Subspace (LCS)**.

To understand LCS structure, we project the averaged latents $\bar{\mathbf{z}}^n$ into this subspace, yielding the average *color coordinates*

$$\bar{\mathbf{c}}^n = \mathbf{B}^\top (\bar{\mathbf{z}}^n - \boldsymbol{\mu}) \in \mathbb{R}^3, \quad n \in 1, \dots, N.$$

These coordinates reveal well-organized geometry (Figure 2). The first dimension spans light to dark, while the second and third jointly form a circular hue structure, with radius encoding saturation. Together, this geometry closely resembles the HSL color representation, organized in a bi-cone. This represents hue as an angle, saturation as the distance from the center, and lightness as an axis.

3.3. Development of Color over Time During Diffusion

Next we analyze how color representations change over time in the FM model with the prompt “yellow and blue checkered tiles”. We project the latent representations from various steps into the LCS, focusing on the hue dimensions (Figure 3a). Each latent patch is a dot in its eventual color, with six colored stars as reference points from $t = 50$. Latent patches start as a centered, color-mixed Gaussian and gradually cluster toward blue, yellow, and brown, showing smooth evolution toward the final colors from early steps.

To quantify the expected position of latent patches at each

timestep given the final color, we generate 26 plain images of differently colored walls with the prompt “{color} wall” (see Appendix A for full color list). We then project each timestep’s latents into the LCS, represent the image with the average of its patches, and visualize the results in Figure 3b. We observe vectors gradually moving outward from the origin, as the FM distribution requires latent patches to start near mid-grey and traverse dimensions that happen to mainly correspond to saturation and lightness in the VAE latent space as they move to their final color. Hence, in the context of the FM model, we interpret these dimensions as additionally relating to the timestep: more specifically, the timestep determines how far along its trajectory toward the final point a latent patch has progressed.

To capture a color’s expected LCS position at timestep t , we must account for the distribution’s time-dependent dynamics, independent of the generated colors. To this end, for each t we compute two statistics: shift $\boldsymbol{\alpha}_t \in \mathbb{R}^3$ and per-axis scale $\boldsymbol{\beta}_t \in \mathbb{R}^3$ describing movement and expansion. We use the 26 images $\{X_i\}_{i=1}^{26}$ from the earlier qualitative analysis and project their token-averaged latents $\bar{\mathbf{z}}_t^i$ from timestep t into LCS. The shift is computed as mean over images $\boldsymbol{\alpha}_t = \frac{1}{N} \sum_{i=1}^N \bar{\mathbf{z}}_t^i$ and scales as mean magnitudes after centering at $\boldsymbol{\alpha}_t$, that is $\boldsymbol{\beta}_t = \frac{1}{N} \sum_{i=1}^N |\bar{\mathbf{z}}_t^i - \boldsymbol{\alpha}_t|$. We report the values of these statistics in the Appendix.

4. Using the Latent Color Subspace

From our analysis in Section 3.2, we assume there exists a bijection between LCS and HSL. We propose an approximation of this mapping from a small set of known correspondences. We evaluate this approximation in two ways: observation and intervention. We show how to observe color directly in latent space mid-generation and intervene on latent representations to achieve a target HSL color.

4.1. Mapping Between Latent Color Subspace and HSL

We construct an approximation of assumed bijective mapping between the LCS coordinates $\mathbf{c} \in \mathbb{R}^3$ and HSL coordinates (h, s, l) using a small set of canonical anchors $\mathcal{A} = \{\mathbf{h}_0, \dots, \mathbf{h}_5, \mathbf{b}, \mathbf{w}\}$. The anchors correspond to six hues (red, blue, green, magenta, cyan, yellow) and black/white extremes. They are obtained by encoding plain color images into VAE latent space and projecting into LCS.

Decoding LCS \rightarrow HSL Given a coordinate \mathbf{c} , the lightness l is obtained by projecting \mathbf{c} onto the achromatic axis $\mathbf{a} := \mathbf{w} - \mathbf{b}$, yielding the projected point \mathbf{c}_L :

$$l = \frac{(\mathbf{c} - \mathbf{b}) \cdot \mathbf{a}}{\|\mathbf{a}\|^2}, \quad \mathbf{c}_L = \mathbf{b} + l\mathbf{a},$$

where \mathbf{b} is the anchor that is origin of the achromatic axis. The hue h is determined along the polygon defined by the six

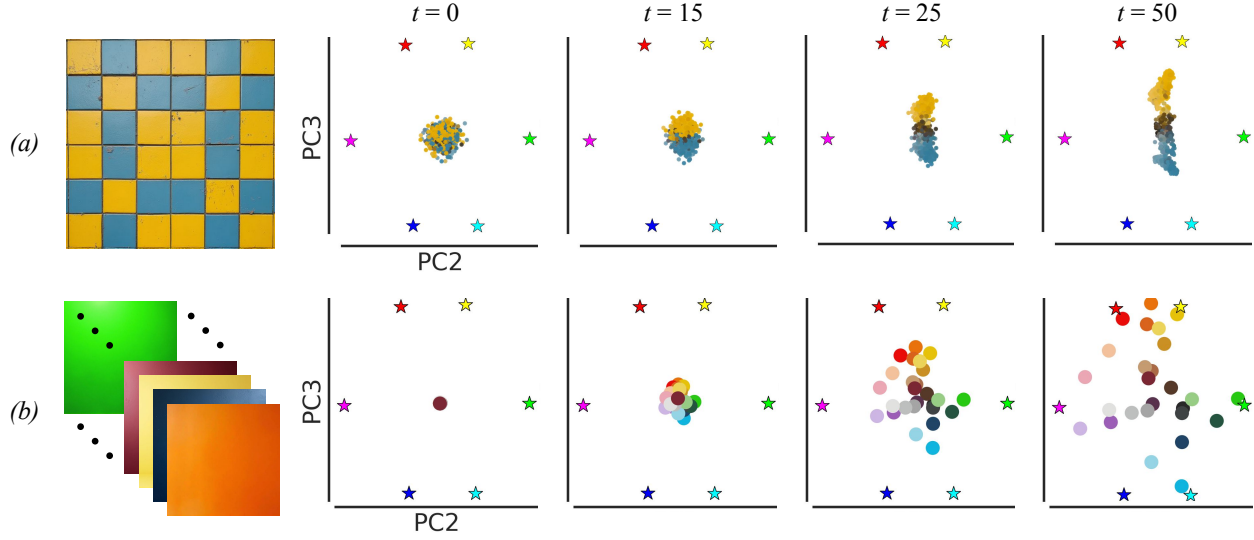


Figure 3. Flow Matching introduces an additional layer of complexity to our interpretation, as latents traverse the space over timesteps to reach their final destination. (a) In the Latent Color Subspace (LCS), colors evolve over timesteps t , starting mixed at the center and gradually moving toward their final positions. Dots represent individual patches, indicated in their ultimate colors, while stars orient the space with known color locations at $t = 50$. (b) Despite variation in individual patches, the *expected* relative position between colors stays consistent over timesteps in the LCS, but scaled with time. Shown on per-image averaged patches (circle) of 26 single-colored images.

hue anchors. Let $\theta_0, \dots, \theta_5$ denote the hue angles of these anchors. We identify the segment $[\theta_k, \theta_{k+1}]$ containing the hue of \mathbf{c} , and interpolate along that edge:

$$h = \theta_k + \alpha(\theta_{k+1} - \theta_k), \quad \alpha = \frac{\angle(\mathbf{c} - \mathbf{c}_L) - \theta_k}{\theta_{k+1} - \theta_k},$$

where $\angle(\mathbf{c} - \mathbf{c}_L)$ is the angle of the chromatic vector relative to the achromatic axis. The corresponding point on the hue polygon is then

$$\mathbf{c}_H = \mathbf{h}_k + \alpha(\mathbf{h}_{k+1} - \mathbf{h}_k)$$

Saturation s is the distance from the lightness axis, normalized by the maximum chroma at that lightness in a bicone:

$$s = \frac{\|\mathbf{c} - \mathbf{c}_L\|}{\|\mathbf{c}_H - \mathbf{c}_L\| (1 - |2l - 1|)}$$

Together, this defines the decoding function D

$$(h, s, l) = D(\mathbf{c})$$

Encoding HSL \rightarrow LCS Given HSL coordinates (h, s, l) , the corresponding point in LCS is reconstructed using the same geometric principles in reverse. The lightness is placed along the achromatic axis:

$$\mathbf{c}_L = \mathbf{b} + la.$$

The hue sets a target point along the polygonal hue path:

$$\mathbf{c}_H = \mathbf{h}_k + \alpha(\mathbf{h}_{k+1} - \mathbf{h}_k), \quad \alpha = \frac{h - \theta_k}{\theta_{k+1} - \theta_k}.$$

Finally, the point is positioned along the radial direction from the achromatic base to the hue point, scaled by the saturation and the chroma limit:

$$\mathbf{c} = \mathbf{c}_L + s (1 - |2l - 1|) (\mathbf{c}_H - \mathbf{c}_L)$$

This defines the encoding function:

$$\mathbf{c} = E(h, s, l).$$

Taken together, D and E can approximate a mapping $\mathbf{c} \leftrightarrow (h, s, l)$, providing access to an interpretable, and well-organized LCS hidden inside the model.

4.2. Mid-Generation Color Observation

We can observe the colors which model is most likely to generate in the final image directly from LCS-projected latent $\mathbf{C} = [\mathbf{c}_i]_{i=1}^L \in \mathbb{R}^{L \times 3}$ at timestep t with our decoding function D . However we have to remember that D is defined in the default VAE latent space (i.e., at the final timestep), and in Section 3.3 we have shown that the statistics of the distribution in LCS change over time. Hence, we start by computing the coordinates normalized to timestep t_{50} :

$$\hat{\mathbf{C}} := [\hat{\mathbf{c}}_i]_{i=1}^L \in \mathbb{R}^{L \times 3}, \quad \hat{\mathbf{c}}_i = \frac{\mathbf{c}_i - \boldsymbol{\alpha}_t}{\boldsymbol{\beta}_t} \odot \boldsymbol{\beta}_{50} + \boldsymbol{\alpha}_{50}$$

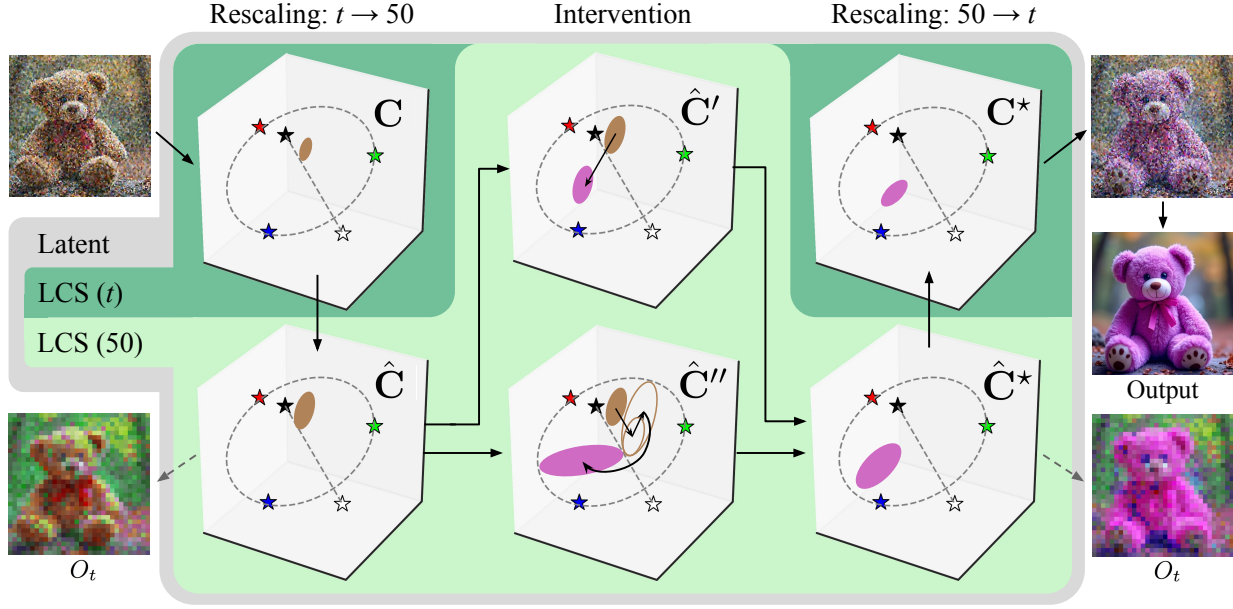


Figure 4. The Latent Color Subspace (LCS) enables observation and intervention during generation. At intermediate timestep t , we project the mid-generated sample from the FM VAE latent space (\square) into the LCS (\blacksquare) obtaining coordinates \mathbf{C} and rescaling them to $\hat{\mathbf{C}}$, which matches timestep $t = 50$ statistics (\blacksquare). Type I intervention ($\hat{\mathbf{C}}'$) modifies color by shifting, scaling, rotating to match the lightness, saturation, and hue respectively, while Type II intervention ($\hat{\mathbf{C}}''$) directly shifts to adjust all three. The interventions are interpolated to get $\hat{\mathbf{C}}^*$ and rescaled back to timestep t (\mathbf{C}^*). Finally \mathbf{C} is replaced with \mathbf{C}^* in the latent of the generated sample. With a simple projection into the LCS and the correct scaling, we can directly observe color (O_t) without the computationally heavy VAE decoder.

Each normalized coordinate $\hat{\mathbf{c}}_t$ is mapped to (h, s, l) using the function D . The results are arranged in a grid to produce a patch-level visualization O_t of color at timestep t .

4.3. Intuition for Color Intervention

Although understanding how the model represents and processes color could enable color manipulation, how and when to intervene remains unclear. FM traverses from the noise to image distribution, with each end of the process implying a fundamentally different way to manipulate color.

At late timesteps, patch colors are fixed, and interventions must preserve inter-patch relations while remaining closed on the LCS. Hence, we shift the mean of the patches to the target color in the HSL space. In the LCS, this translates to adjusting hue, saturation, and lightness via rotation, shrinkage, and shift along the black-white axis, respectively.

However, color is not yet a property of individual patches early on. LCS coordinates of patches form an unstructured cloud where variance reflects unresolved possibilities, not color differences. Shrinkage collapses variance, destroying diversity instead of yielding coherent color changes. The mean decodes near grey by construction, rendering rotation largely ineffective for altering hue. But as Figure 3 shows, the patch coordinates' mean captures color, so a uniform

distribution shift should achieve the desired color change.

Since FM treats the trajectory as an interpolation between image and noise, we interpolate between the color interventions with the same proportions. Section 5 qualitatively examines these two strategies and their interpolation.

4.4. Concretizing Color Intervention

We consider a target color $\mathbf{y}^* = (h^*, s^*, l^*)$ in HSL format and its application at timestep t to the LCS coordinates of image patches. Let $\mathbf{C} := [\mathbf{c}_i]_{i=0}^L \in \mathbb{R}^{L \times 3}$ denote the collection of L patch coordinates at timestep t . To utilize the LCS-HSL approximation, we first normalize coordinates \mathbf{C} to a reference timestep t_{50} , obtaining $\hat{\mathbf{C}} := [\hat{\mathbf{c}}_i]_{i=0}^L \in \mathbb{R}^{L \times 3}$. We now shift all patches to the desired color via the same intervention. Two types of interventions can achieve this.

Type I: Direct LCS translation We can compute the mean of the normalized coordinates $\bar{\mathbf{c}} = \frac{1}{L} \sum_{i=1}^L \hat{\mathbf{c}}_i$, encode the target color to LCS coordinates $\mathbf{c}^* = E(\mathbf{y}^*)$, and shift all patches by the same offset to get shifted coordinates

$$\hat{\mathbf{C}}' := [\hat{\mathbf{c}}'_i]_{i=0}^L, \quad \hat{\mathbf{c}}'_i = \hat{\mathbf{c}}_i + (\mathbf{c}^* - \bar{\mathbf{c}}).$$

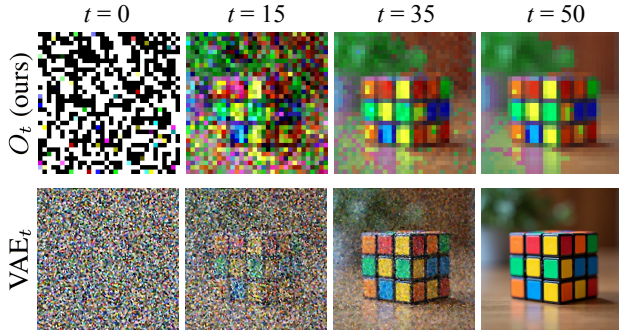


Figure 5. With our mid-generation color observation method (top), we validate our interpretation of the Latent Color Subspace (LCS) by predicting the final colors at intermediate timesteps. We compare these predictions with the VAE-decoded latents (bottom).

Type II: LCS shift via HSL space Alternatively, we can decode $\hat{\mathbf{C}}$ to HSL colors:

$$\mathbf{Y} := [\mathbf{y}_i]_{i=0}^L, \quad \mathbf{y}_i = D(\hat{\mathbf{c}}_i).$$

Then, obtain mean HSL color across patches, $\bar{\mathbf{y}} = \frac{1}{L} \sum_{i=1}^L \mathbf{y}_i$, and shift each patch in HSL space to produce the shifted HSL colors

$$\mathbf{Y}'' := [\mathbf{y}_i'']_{i=0}^L, \quad \mathbf{y}_i'' = \mathbf{y}_i + (\mathbf{y}^* - \bar{\mathbf{y}}).$$

Encoding yields shifted LCS coordinates $\hat{\mathbf{C}}'' = E(\mathbf{Y}'')$.

We can also interpolate between both intervention types defining shifted LCS coordinates as

$$\hat{\mathbf{C}}^* := \gamma_t \cdot \hat{\mathbf{C}}' + (1 - \gamma_t) \cdot \hat{\mathbf{C}}'',$$

where γ is timestep-dependent interpolation coefficient derived from the FM scheduler. For all interventions, the resulting shifted LCS coordinates $\hat{\mathbf{C}}'$, $\hat{\mathbf{C}}''$, $\hat{\mathbf{C}}^*$ are denormalized back to timestep t , giving the final modified coordinates \mathbf{C}' , \mathbf{C}'' , \mathbf{C}^* . We say we apply Type I/Type II/interpolated intervention when we replace the original coordinates \mathbf{C} with $\mathbf{C}'/\mathbf{C}''/\mathbf{C}^*$. This process can be visualized in Figure 4.

Object-Localized Color Intervention To alter the color of individual objects (specific patches), we leverage segmentation maps derived from text-image cross-attention (Kim et al., 2025a), selecting transformer layer 18.

5. Experiments

We measure perceptual color difference with HSL error (ΔH , ΔS , ΔL), with H in degrees and S and L as percentages, and CIEDE2000 (Luo et al., 2001) (ΔE_{00}). Figure 6 presents Type I (c) and Type II (a) interventions; all remaining results use the interpolation strategy at timestep 9.

Table 1. Perceptual color difference (ΔE_{00}) between final images and latents at timestep t , observed by VAE-decoding (VAE_t) and interpreting the LCS (O_t). Note that by FLUX’s design, VAE_{50} is the final image and latents at $t = 0$ are pure noise.

		(a) ΔE_{00} computed per pixel					
Dataset	Method	0	10	t		40	50
OBJECTS	O_t (ours)	40	31	21	16	14	14
	VAE_t	26	21	15	9	4	0
WALLS	O_t (ours)	46	29	19	15	13	13
	VAE_t	31	23	16	9	4	0

		(b) ΔE_{00} computed for average pixel					
Dataset	Method	0	10	t		40	50
OBJECTS	O_t (ours)	16	8	10	10	10	10
	VAE_t	16	13	10	6	3	0
WALLS	O_t (ours)	28	8	10	11	11	12
	VAE_t	27	20	14	8	3	0

5.1. Observation: Qualitative Evaluation

Figure 5 shows our observation method on the prompt “a photo of a rubik’s cube on a table” across four timesteps. For comparison, we decode the corresponding latents with the VAE. Our method allows emerging colors to be clearly observed directly in latent space without decoding. Moreover, the accuracy with which we predict the final colors closely mirrors the fidelity of the decoded images, indicating the method reliably captures up-to-date information about the color dynamics occurring within the latent space at each timestep. More examples can be found in the Appendix.

5.2. Observation: Quantitative Evaluation

In Table 1, we quantitatively evaluate how accurately our observation method represents the downscaled final image with ΔE_{00} . We compare this to how well direct decoding of the latent with the VAE decoder represents the final image. We evaluate on two datasets: (i) GenEval’s single-object task, scaling to more complex images, and (ii) a dataset of 26 plain-colored walls described in Section 3.

At $t = 50$, our method achieves low color prediction errors of $\Delta E_{00} \leq 14$ on both datasets, for both per-pixel and averaged evaluations. In the per-pixel setting, errors fall to $\Delta E_{00} \leq 21$ as early as $t = 20$. But as expected, early timesteps are dominated by noise, resulting in less accurate predictions. In the averaged setting, performance is particularly strong: we obtain $\Delta E_{00} \leq 12$ on both datasets for all timesteps $t > 0$. Notably, for $t \leq 20$, our method even outperforms direct VAE decoding on both datasets. This suggests that our approach more effectively leverages the information encoded in global latent statistics, whereas the

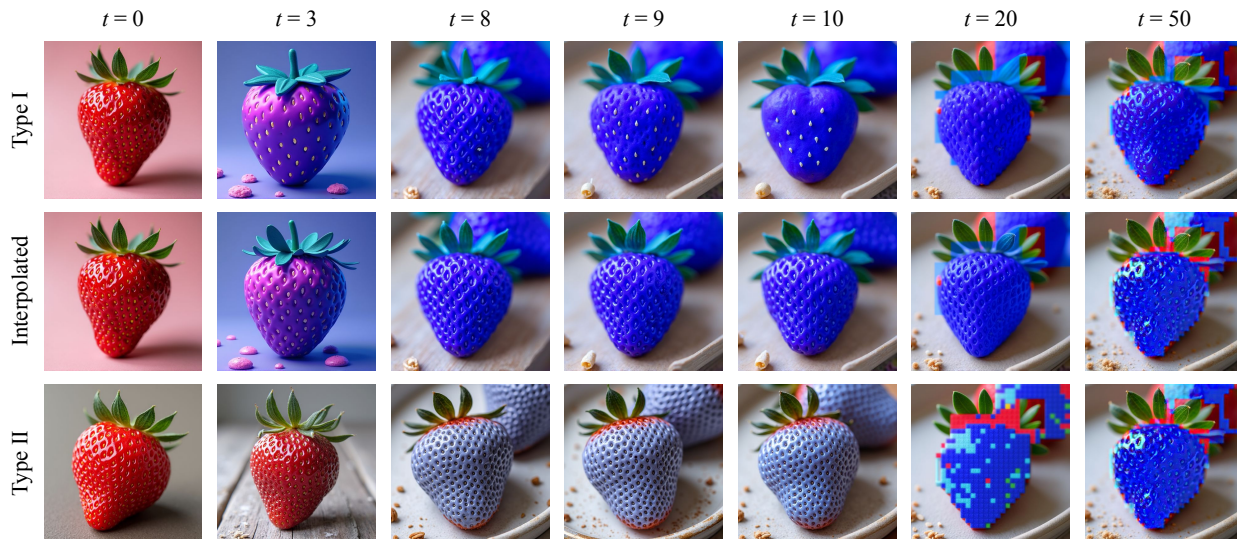


Figure 6. Color intervention shifting latent patches directly in LCS (Type I) disrupts texture, whereas shifting them via HSL (Type II) may have limited impact at early timesteps. Interpolating enables accurate color changes while preserving texture.

Table 2. Accuracy of our color intervention with GENEVAL’s color task and the PRECISE tasks, including natural / plain images in 51 colors. We measure CIEDE2000 (ΔE_{00}) and average distances in hue (ΔH), saturation (ΔS), and lightness (ΔL) from target color. As baseline, we include results without specifying colors in the prompts (None). Our method effectively alters colors, affecting either entire image (global) or target object (local), without modifying this prompt. For comparison, we include color injected via prompt (Prompt).

Color Injection	GENEVAL Acc (\uparrow)	PRECISE (NATURAL)				PRECISE (PLAIN)			
		ΔE_{00} (\downarrow)	ΔH (\downarrow)	ΔS (\downarrow)	ΔL (\downarrow)	ΔE_{00} (\downarrow)	ΔH (\downarrow)	ΔS (\downarrow)	ΔL (\downarrow)
None	9%	40	90°	48%	21%	35	89°	56%	22%
Prompt	79%	25	41°	31%	14%	22	38°	29%	12%
Ours local	70%	17	24°	29%	8%	-	-	-	-
Ours global	73%	21	26°	26%	12%	9	11°	25%	3%

VAE decoder is trained only to decode the final latent representation. With our method, all of these quantities can be predicted directly in the latent space, without requiring the 50-million-parameter decoder to reconstruct the image.

5.3. Intervention: Qualitative Evaluation

As discussed in Section 4.4, Figure 6 considers three strategies for handling patches in latent space: Type I, Type II, and interpolation. We find interpolation at timesteps 8 – 10 most effective. In Type I, interventions can lose texture if applied too late (see $t = 10$), likely from unintended saturation changes; at very late timesteps, color fails to integrate and instead appears as a thin surface layer (see $t = 50$). In contrast, Type II can have little influence on the final image when applied at early timesteps (see $t = 3$). More generally, reliance on the model’s internal, attention-based segmentation limits the feasibility of very early interventions (see $t = 3$ Type I), while the need for subsequent model “cleaning” to remove artifacts (see $t = 20$ Type II) and to smooth sharp, patch-induced boundaries (see $t = 50$) makes late interventions undesirable. Our proposed interpolation approach addresses these limitations. In the critical

timestep range effective for modifications (see $t = 8$ – 10), interpolation enables color integration while preserving more fine-grained texture than either Type I or II alone.

In Figure 7, we showcase our interpolated color-intervention method on four prompts (“a photo of a teddy bear,” “a photo of a shoe,” “a photo of a flower,” “a photo of a parrot”) and six colors. Here, our method accurately identifies and manipulates individual objects’ color while preserving overall structure. When applied to multi-color objects (see parrot), our method modifies the object so significant portions adopt the target color while remaining multi-colored overall. Appendix B showcases our method’s ability to generate fine-grained, novel hues and to control saturation and lightness.

5.4. Intervention: Quantitative Evaluation

Table 2 evaluates our intervention. As a baseline, we use FLUX with prompts specifying only objects, without color (None). Without modifying the prompt, our method injects color in two settings: global changes affecting the entire image and local changes applied only to the target object. We compare to prompt-based color injection. We report ac-



Figure 7. With our latent-space color interpretation, we can accurately guide objects toward target colors (top) while preserving much of the original image’s high-level structure (left). Even multi-colored objects retain color diversity while shifting toward the target (bottom).

Table 3. Measured against the base prompt, we preserve original image structure more faithfully than prompt-based color changes.

Color Inj.	IOU (\uparrow)	SSIM (\uparrow)	LPIPS (\downarrow)	DINOv2 (\downarrow)
Prompt	0.60	0.46	0.49	0.36
Ours local	0.78	0.59	0.35	0.29
Ours global	0.88	0.56	0.36	0.23

curacy on GenEval’s *color* task (Ghosh et al., 2023) (see Appendix). Precise color control is not yet a well-established task, so existing benchmarks are limited; for more precise color measurements, we use 4,080 natural-images with 20 GenEval objects, 51 HSL colors, and 4 seeds (PRECISE (NATURAL), see Appendix). We isolate the object with masks from GenEval’s object detector and compare the average masked color to the target color. For simpler images, we use 10 prompt-seed pairs that get plain images (PRECISE (PLAIN), see Appendix), without segmentation.

Mechanistic control alone raises the color accuracy from 9% to 73% on GenEval without changing the prompt, and approaches the 79% achievable with color-explicit prompts. Local changes achieve 70%, showing minimal error from segmentation masks. In PRECISE, our method has very accurate color control on plain images, with $\Delta E_{00} = 9$, $\Delta H = 11^\circ$, and $\Delta L = 3\%$, compared to prompt-only results of $\Delta E_{00} = 22$, $\Delta H = 38^\circ$, and $\Delta L = 12\%$. Even

on complex images with local masks, accuracy remains high, with $\Delta E_{00} = 17$ and $\Delta H = 24^\circ$. Overall, our approach achieves color precision beyond what prompting alone can provide, especially in hue.

5.5. Intervention Impact on Image Structure

On GenEval’s color task, we examine how much our method alters image structure relative to the base generation, comparing it to prompt-based color changes with three similarity metrics: SSIM (Wang et al., 2004), LPIPS (Zhang et al., 2018) and distance in DINOv2 feature space (Oquab et al., 2023), all applied in grayscale to ignore the color. We also measure IoU between object masks from GenEval’s detector. On all four metrics, our method more closely preserves the original image structure than modifying color via prompt. See Appendix for qualitative comparison.

6. Conclusion

We find that color is represented in the VAE latent space of FLUX as an HSL-like bicone. We show that the corresponding latent directions can be used to both observe and intervene upon the generative process. We propose a fully training-free color-intervention method that enables control through purely mechanistic latent-space manipulation.

7. Acknowledgments

This work was partially funded by the ERC (853489 - DEXIM) and the Alfred Krupp von Bohlen und Halbach Foundation, which we thank for their generous support. We are also grateful for partial support from the Pioneer Centre for AI, DNRF grant number P1. Mateusz Pach would like to thank the European Laboratory for Learning and Intelligent Systems (ELLIS) PhD program for support. The authors gratefully acknowledge the scientific support and resources of the AI service infrastructure LRZ AI Systems provided by the Leibniz Supercomputing Centre (LRZ) of the Bavarian Academy of Sciences and Humanities (BAdW), funded by Bayerisches Staatsministerium für Wissenschaft und Kunst (StMWK).

References

- Albergo, M. S. and Vanden-Eijnden, E. Building normalizing flows with stochastic interpolants. In *ICLR*, 2023.
- Arias, G., Sola, A., Armengod, M., and Vanrell, M. Color encoding in latent space of stable diffusion models. 2025.
- Bader, J., Girrbach, L., Alaniz, S., and Akata, Z. Sub: Benchmarking cbm generalization via synthetic attribute substitutions. *ICCV*, 2025a.
- Bader, J., Pach, M., Bravo, M. A., Belongie, S., and Akata, Z. Stitch: Training-free position control in multimodal diffusion transformers. *arXiv*, 2025b.
- BlackForest. Flux. <https://github.com/black-forest-labs/flux>, 2024.
- Butt, M. A., Wang, K., Vazquez-Corral, J., and van de Weijer, J. Colorpeel: Color prompt learning with diffusion models via color and shape disentanglement. In *ECCV*, 2024.
- Chefer, H., Alaluf, Y., Vinker, Y., Wolf, L., and Cohen-Or, D. Attend-and-excite: Attention-based semantic guidance for text-to-image diffusion models. In *ACM Transactions on Graphics (TOG)*, 2023.
- Chen, J., Yu, J., Ge, C., Yao, L., Xie, E., Wang, Z., Kwok, J. T., Luo, P., Lu, H., and Li, Z. Pixart- α : Fast training of diffusion transformer for photorealistic text-to-image synthesis. In *ICLR*, 2024.
- Daujotas, G. Interpreting and steering features in images. In *LessWrong*, 2024.
- DeepMind, G. Imagen 4. <https://deepmind.google/models/imagen/>, 2025.
- Dinkevich, D., Levy, M., Avrahami, O., Samuel, D., and Lischinski, D. Story2board: A training-free approach for expressive storyboard generation. *arXiv*, 2025.
- Esser, P., Kulal, S., Blattmann, A., Entezari, R., Müller, J., Saini, H., Levi, Y., Lorenz, D., Sauer, A., Boesel, F., et al. Scaling rectified flow transformers for high-resolution image synthesis. In *ICML*, 2024.
- Eyring, L., Karthik, S., Dosovitskiy, A., Ruiz, N., and Akata, Z. Noise hypernetworks: Amortizing test-time compute in diffusion models. *NeurIPS*, 2025.
- Eyring, L. V., Karthik, S., Roth, K., Dosovitskiy, A., and Akata, Z. Reno: Enhancing one-step text-to-image models through reward-based noise optimization. *NeurIPS*, 2024.
- Farshad, A., Yeganeh, Y., Chi, Y., Shen, C., Ommer, B., and Navab, N. Scenegenie: Scene graph guided diffusion models for image synthesis. In *ICCV*, 2023.
- Ghosh, D., Hajishirzi, H., and Schmidt, L. Geneval: An object-focused framework for evaluating text-to-image alignment. *NeurIPS*, 2023.
- Helbling, A., Meral, T. H. S., Hoover, B., Yanardag, P., and Chau, D. H. Conceptattention: Diffusion transformers learn highly interpretable features, 2025.
- Hertz, A., Mokady, R., Tenenbaum, J., Aberman, K., Pritch, Y., and Cohen-or, D. Prompt-to-prompt image editing with cross-attention control. In *ICLR*, 2023.
- Hu, Y., Peng, J., Lin, Y., Liu, T., Qu, X., Liu, L., Zhao, Y., and Wei, Y. Dcredit: Dual-level controlled image editing via precisely localized semantics, 2025.
- Kim, C., Shin, H., Hong, E., Yoon, H., Arnab, A., Seo, P. H., Hon, S., and Kim, S. Seg4diff: Unveiling open-vocabulary segmentation in text-to-image diffusion transformers. In *NeurIPS*, 2025a.
- Kim, D., Thomas, X., and Ghadiyaram, D. Revelio: Interpreting and leveraging semantic information in diffusion models. In *ICCV*, 2025b.
- Kingma, D. P. and Welling, M. Auto-encoding variational bayes. 2014.
- Labs, B. F., Batifol, S., Blattmann, A., Boesel, F., Consul, S., Diagne, C., Dockhorn, T., English, J., English, Z., Esser, P., Kulal, S., Lacey, K., Levi, Y., Li, C., Lorenz, D., Müller, J., Podell, D., Rombach, R., Saini, H., Sauer, A., and Smith, L. Flux.1 kontext: Flow matching for in-context image generation and editing in latent space, 2025.
- Li, Y., Liu, H., Wu, Q., Mu, F., Yang, J., Gao, J., Li, C., and Lee, Y. J. Gligen: Open-set grounded text-to-image generation. *CVPR*, 2023.

- Liang, Z., Li, Z., Zhou, S., Li, C., and Loy, C. C. Control color: Multimodal diffusion-based interactive image colorization. 2025.
- Lipman, Y., Chen, R. T., Ben-Hamu, H., Nickel, M., and Le, M. Flow matching for generative modeling. *arXiv*, 2022.
- Liu, X., Gong, C., and Liu, Q. Flow straight and fast: Learning to generate and transfer data with rectified flow. In *ICLR*, 2023.
- Liu, Y., Bader, J., and Kim, J. M. Does feasibility matter? understanding the impact of feasibility on synthetic training data. *FGVC Workshop at CVPR*, 2025.
- Luo, M. R., Cui, G., and Rigg, B. The development of the cie 2000 colour-difference formula: Ciede2000. *Color Research & Application: Endorsed by Inter-Society Color Council, The Colour Group (Great Britain), Canadian Society for Color, Color Science Association of Japan, Dutch Society for the Study of Color, The Swedish Colour Centre Foundation, Colour Society of Australia, Centre Français de la Couleur*, 26(5):340–350, 2001.
- Mantecon, H. L., Gomez-Villa, A., Qin, J., Butt, M. A., Raducanu, B., Vazquez-Corral, J., van de Weijer, J., and Wang, K. Leveraging semantic attribute binding for free-lunch color control in diffusion models. *WACV*, 2026.
- Midjourney. midjourney v7, 2025. URL <https://github.com/midjourney>.
- Niedoba, M., Zwartsenberg, B., Murphy, K. P., and Wood, F. Towards a mechanistic explanation of diffusion model generalization. In *ICML*, 2025.
- Oorloff, T., Sindagi, V., Bandara, W. G. C., Shafahi, A., Ghiasi, A., Prakash, C., and Ardekani, R. Stable diffusion models are secretly good at visual in-context learning. *ICCV*, 2025.
- OpenAI. DALL-E 3. <https://openai.com/research/dall-e-3>, September 2023.
- Oquab, M., Darcet, T., Moutakanni, T., Vo, H. V., Szafraniec, M., Khalidov, V., Fernandez, P., Haziza, D., Massa, F., El-Nouby, A., Howes, R., Huang, P.-Y., Xu, H., Sharma, V., Li, S.-W., Galuba, W., Rabbat, M., Assran, M., Ballas, N., Synnaeve, G., Misra, I., Jegou, H., Mairal, J., Labatut, P., Joulin, A., and Bojanowski, P. Dinov2: Learning robust visual features without supervision, 2023.
- Peebles, W. and Xie, S. Scalable diffusion models with transformers. In *ICCV*, 2023.
- Podell, D., English, Z., Lacey, K., Blattmann, A., Dockhorn, T., Muller, J., Penna, J., and Rombach, R. Sdxl: Improving latent diffusion models for high-resolution image synthesis. *arXiv*, 2023.
- Rombach, R., Blattmann, A., Lorenz, D., Esser, P., and Ommer, B. High-resolution image synthesis with latent diffusion models. *CVPR*, 2022.
- Shabalina, S., Kharlapenko, D., Panda, A., Ali, S. A. R., Hao, Y., and Conmy, A. Interpreting large text-to-image diffusion models with dictionary learning. In *Mechanistic Interpretability for Vision at CVPR (Non-proceedings Track)*, 2025.
- Shi, Y., Li, C., Wang, Y., Xiang Zhao, Y., Pang, A., Yang, S., Yu, J., and Ren, K. Dissecting and mitigating diffusion bias via mechanistic interpretability. In *CVPR*, 2025.
- Shum, K. C., Hua, B.-S., Nguyen, D. T., and Yeung, S.-K. Color alignment in diffusion. 2025a.
- Shum, K. C., Hua, B.-S., Nguyen, D. T., and Yeung, S.-K. Color alignment in diffusion. In *CVPR*, 2025b.
- Tang, R., Liu, L., Pandey, A., Jiang, Z., Yang, G., Kumar, K., Stenetorp, P., Lin, J., , and Ture, F. What the daam: Interpreting stable diffusion using cross attention. In *Annual Meeting of the Association for Computational Linguistics (Volume 1: Long Papers)*, 2023.
- Vavilala, V., Shaik, F., and Forsyth, D. Dequantization and color transfer with diffusion models. 2025.
- Wang, B., Fan, J., and Pan, X. Circuit mechanisms for spatial relation generation in diffusion transformers. In *arXiv*, 2026.
- Wang, Q., Liang, Y., Zheng, Y., Xu, K., Zhao, J., and Wang, S. Generative ai for urban planning: Synthesizing satellite imagery via diffusion models. *Computers, Environment and Urban Systems*, 122:102339, 2025. ISSN 0198-9715.
- Wang, Z., Bovik, A. C., Sheikh, H. R., and Simoncelli, E. P. Image quality assessment: from error visibility to structural similarity. *IEEE transactions on image processing*, 13(4):600–612, 2004.
- Wu, C., Li, J., Zhou, J., Lin, J., Gao, K., Yan, K., Yin, S.-m., Bai, S., Xu, X., Chen, Y., et al. Qwen-image technical report. *arXiv preprint arXiv:2508.02324*, 2025.
- Yang, Y., Chang, D., Fang, Y., Song, Y.-Z., Ma, Z., and Guo, J. Controllable-continuous color editing in diffusion model via color mapping. In *arXiv*, 2025.
- Ye, H., Zhang, J., Liu, S., Han, X., and Yang, W. Ip-adapter: Text compatible image prompt adapter for text-to-image diffusion models. *arXiv*, 2023.
- Yellapragada, S., Graikos, A., Prasanna, P., Kurc, T., Saltz, J., and Samaras, D. Pathldm: Text conditioned latent diffusion model for histopathology. In *WACV*, 2024.

- Zhang, L., Rao, A., and Agrawala, M. Adding conditional control to text-to-image diffusion models. *ICCV*, 2023a.
- Zhang, L., Rao, A., and Agrawala, M. Adding conditional control to text-to-image diffusion models. In *ICCV*, 2023b.
- Zhang, R., Isola, P., Efros, A. A., Shechtman, E., and Wang, O. The unreasonable effectiveness of deep features as a perceptual metric. In *CVPR*, 2018.
- Zhang, S., Chen, Z., Chen, L., and Wu, Y. Cdst: Color disentangled style transfer for universal style reference customization. 2025.

A. Colors in Timestep Experiments

The following colors are used in the timestep experiments, along with the average HEX value of the color:

Bright red: #D81511
Light red: #E7A0AD
Dark red: #78262F
Bright orange: #EA710B
Light orange: #F3C09C
Dark orange: #AA552F
Bright yellow: #F3DB1B
Light yellow: #ECD25B
Dark yellow: #D69613
Bright green: #26C812
Light green: #8DCF7A
Dark green: #1D4B32
Bright blue: #0FB3DF
Light blue: #94D3E3
Dark blue: #184166
Bright purple: #9360B4
Light purple: #CDB5E4
Dark purple: #59334C
Bright grey: #A3A4A3
Light grey: #BCBFBE
Dark grey: #3F4244
White: #E0E1E0
Black: #292929
Bright brown: #AA6B46
Light brown: #C8A171
Dark brown: #563727

B. Additional Qualitative Results

We further illustrate the flexibility of our interpolated intervention method through additional qualitative examples. Figure 8 demonstrates fine-grained control over predicted hues, spanning a continuous range from red to magenta (#E60000, #E6002E, #E6005C, #E6008A, #E600B8, #E600E6). Figure 9 showcases saturation control by interpolating from blue to grey (#0000CC, #1A1AE6, #3333CC, #4D4DB3, #666699, #808080). Finally, Figure 11 highlights control over lightness, ranging from white to black through red (#DDDDDD, #F2B6B6, #D81612, #990000, #330000, #222222).



Figure 8. Demonstration of our interpolation method’s ability to generate novel hues, spanning red to magenta.

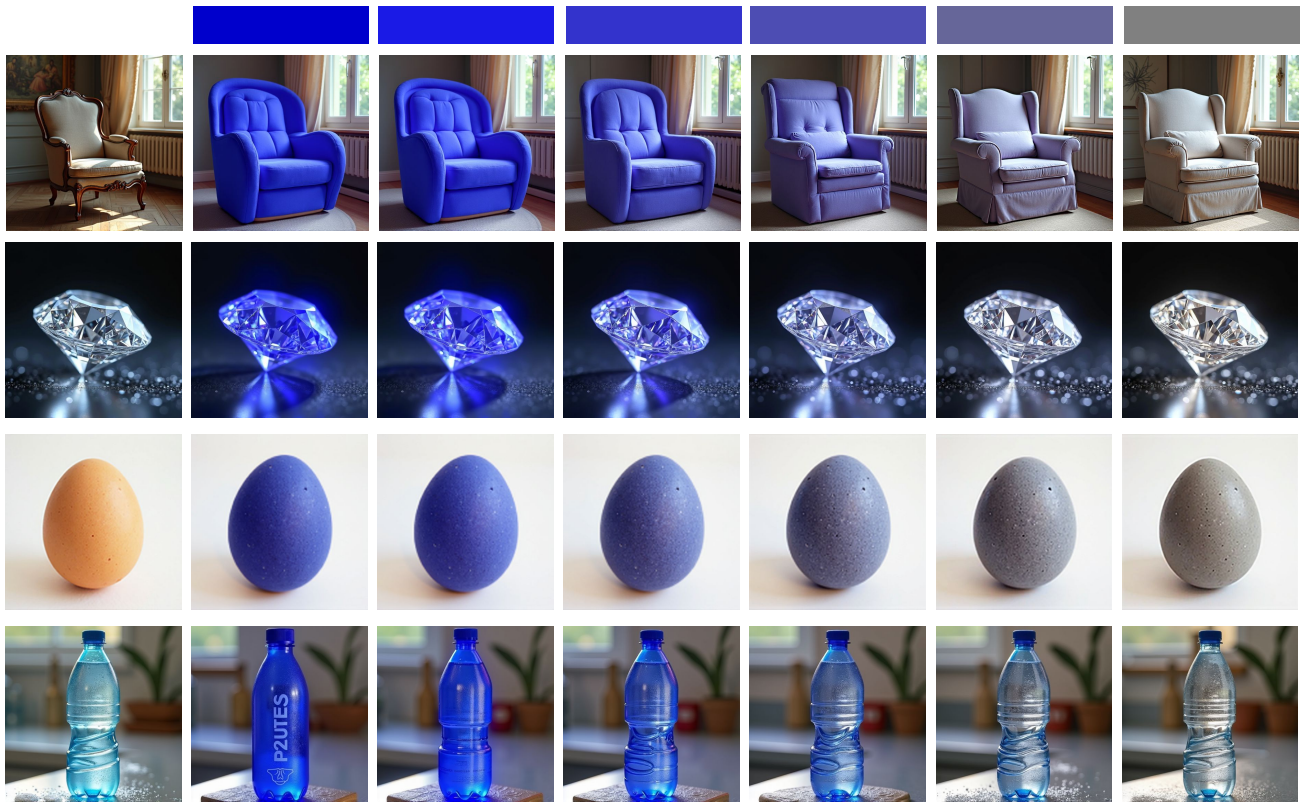


Figure 9. Demonstration of our interpolation method's ability to control saturation, spanning blue to grey.

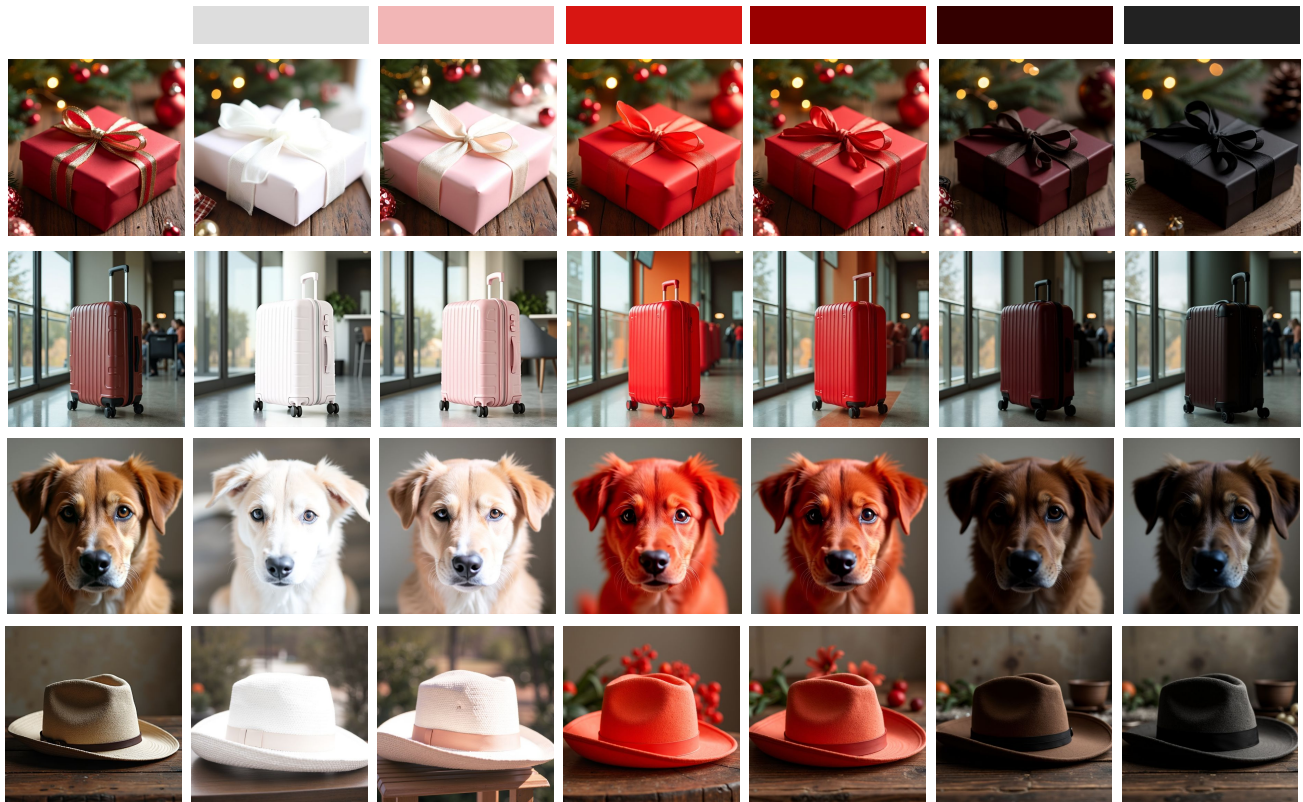


Figure 10. Demonstration of our interpolation method's ability to control lightness, spanning from white to black through red.

C. PRECISE (OBJECTS) Settings

We include 20 objects from GenEval: "a photo of a frisbee", "a photo of a cow", "a photo of a broccoli", "a photo of a scissors", "a photo of a carrot", "a photo of a suitcase", "a photo of an elephant", "a photo of a cake", "a photo of a refrigerator", "a photo of a teddy bear", "a photo of a microwave", "a photo of a sheep", "a photo of a dog", "a photo of a zebra", "a photo of a bird", "a photo of a backpack", "a photo of a skateboard", "a photo of a banana", "a photo of a bear", "a photo of a fire hydrant".

We include a total of 51 colors, with 12 evenly distributed hues, with 4 types applied to each: light, dark, muted (unsaturated), and normal (saturated). The final three colors are black, grey, and white. Colors use following HEX codes and prompt names: 'Red': #FF0000, 'Orange': #FF7F00, 'Yellow': #FFFF00, 'Chartreuse': #7FFF00, 'Green': #00FF00, 'Spring Green': #00FF7F, 'Cyan': #00FFFF, 'Azure': #007FFF, 'Blue': #0000FF, 'Violet': #7F00FF, 'Magenta': #FF00FF, 'Rose': #FF007F, 'Dark Red': #7F0000, 'Dark Orange': #7F3F00, 'Dark Yellow': #7F7F00, 'Dark Chartreuse': #3F7F00, 'Dark Green': #007F00, 'Dark Spring Green': #007F3F, 'Dark Cyan': #007F7F, 'Dark Azure': #003F7F, 'Dark Blue': #00007F, 'Dark Violet': #3F007F, 'Dark Magenta': #7F007F, 'Dark Rose': #7F003F, 'Light Red': #FF7F7F, 'Light Orange': #FFBF7F, 'Light Yellow': #FFFF7F, 'Light Chartreuse': #BFFF7F, 'Light Green': #7FFF7F, 'Light Spring Green': #7FFFBF, 'Light Cyan': #7FFFFFFF, 'Light Azure': #7FBFFF, 'Light Blue': #7F7FFF, 'Light Violet': #BF7FFF, 'Light Magenta': #FF7FFF, 'Light Rose': #FF7FBF, 'Muted Red': #BF4040, 'Muted Orange': #BF7F40, 'Muted Yellow': #BFBF40, 'Muted Chartreuse': #7FBF40, 'Muted Green': #40BF40, 'Muted Spring Green': #40BF7F, 'Muted Cyan': #40BFBF, 'Muted Azure': #407FBF, 'Muted Blue': #4040BF, 'Muted Violet': #7F40BF, 'Muted Magenta': #BF40BF, 'Muted Rose': #BF407F, 'Black': #000000, 'White': #FFFFFF, 'Gray': #808080

Masks are taken from the object detector used for GenEval evaluation.

D. PRECISE (PLAIN) Settings

In this setting, colors remain the same from the OBJECTS setting. Prompt-seed pairings are: ("a close-up photo of a wall", 12), ("a close-up photo of a paper sheet", 8), ("a photo of a clear sky", 4), ("a close-up photo of a plain sweater", 15), ("a close-up photo of a concrete floor", 5), ("a closeup of a plain rug", 3), ("a photo of a clear sky at night", 6), ("a close-up photo of sand", 0), ("a close-up photo of metal texture", 8), ("a close-up photo of wooden texture", 9)

Seeds were selected for uniform images.

E. Additional Qualitative Observation Results

We include additional timesteps, to show our observation method in more detail on the prompt from the main paper, "a photo of a rubik's cube on the table. We show two additional examples as well, "a photo of a christmas tree" and "a photo of a fire truck".

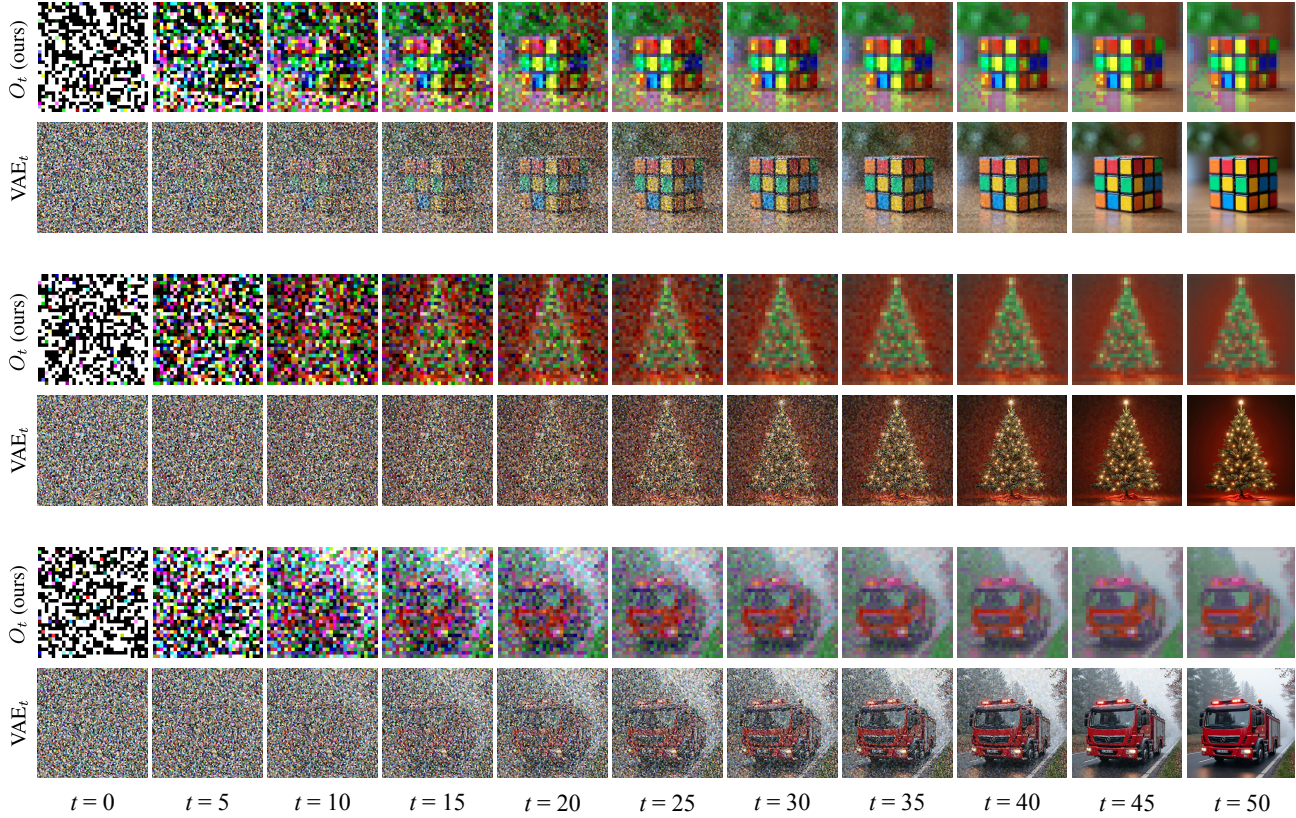


Figure 11. Qualitative examples of our observation method at a variety of timesteps, showcasing the accuracy of our Latent Color Space.

F. Timestep Statistics of the Latent Color Subspace

We calculate the expected shift for each timesteps:

t = 0: 2.3413, -2.3586, 0.4266
t = 1: 2.3574, -2.3833, 0.4644
t = 2: 2.3638, -2.3904, 0.4883
t = 3: 2.3734, -2.3951, 0.5122
t = 4: 2.3831, -2.3993, 0.5384
t = 5: 2.3925, -2.4026, 0.5647
t = 6: 2.4023, -2.4047, 0.5919
t = 7: 2.4124, -2.4060, 0.6198
t = 8: 2.4226, -2.4064, 0.6484
t = 9: 2.4330, -2.4060, 0.6772
t = 10: 2.4437, -2.4051, 0.7065
t = 11: 2.4546, -2.4035, 0.7367
t = 12: 2.4659, -2.4011, 0.7668
t = 13: 2.4775, -2.3981, 0.7974
t = 14: 2.4897, -2.4009, 0.8312
t = 15: 2.5021, -2.4036, 0.8656
t = 16: 2.5148, -2.4065, 0.9008
t = 17: 2.5277, -2.4093, 0.9364
t = 18: 2.5408, -2.4123, 0.9727
t = 19: 2.5542, -2.4154, 1.0099
t = 20: 2.5680, -2.4186, 1.0481
t = 21: 2.5820, -2.4218, 1.0868
t = 22: 2.5963, -2.4252, 1.1263
t = 23: 2.6110, -2.4288, 1.1672
t = 24: 2.6261, -2.4324, 1.2090
t = 25: 2.6416, -2.4363, 1.2520
t = 26: 2.6575, -2.4403, 1.2957
t = 27: 2.6738, -2.4444, 1.3406
t = 28: 2.6904, -2.4485, 1.3865
t = 29: 2.7074, -2.4529, 1.4336
t = 30: 2.7250, -2.4574, 1.4818
t = 31: 2.7432, -2.4621, 1.5314
t = 32: 2.7618, -2.4669, 1.5823
t = 33: 2.7810, -2.4720, 1.6344
t = 34: 2.8006, -2.4771, 1.6878
t = 35: 2.8209, -2.4826, 1.7430
t = 36: 2.8418, -2.4883, 1.7995
t = 37: 2.8631, -2.4944, 1.8578
t = 38: 2.8853, -2.5005, 1.9179
t = 39: 2.9080, -2.5066, 1.9793
t = 40: 2.9313, -2.5132, 2.0426
t = 41: 2.9555, -2.5199, 2.1082
t = 42: 2.9804, -2.5268, 2.1756
t = 43: 3.0060, -2.5338, 2.2450
t = 44: 3.0328, -2.5411, 2.3172
t = 45: 3.0603, -2.5486, 2.3914
t = 46: 3.0889, -2.5561, 2.4682
t = 47: 3.1189, -2.5640, 2.5482
t = 48: 3.1497, -2.5725, 2.6302
t = 49: 3.1824, -2.5796, 2.7175
t = 50: 3.2152, -2.5889, 2.8050

We provide the mean magnitudes after centering as well:

t = 0: 0.0163, 0.0172, 0.0295
t = 1: 0.0905, 0.0716, 0.0999
t = 2: 0.1345, 0.1123, 0.1544
t = 3: 0.1826, 0.1491, 0.2065
t = 4: 0.2360, 0.1899, 0.2630
t = 5: 0.2904, 0.2316, 0.3202
t = 6: 0.3471, 0.2749, 0.3793
t = 7: 0.4050, 0.3191, 0.4394
t = 8: 0.4640, 0.3641, 0.5003
t = 9: 0.5231, 0.4091, 0.5611
t = 10: 0.5834, 0.4547, 0.6228
t = 11: 0.6456, 0.5016, 0.6861
t = 12: 0.7077, 0.5481, 0.7488
t = 13: 0.7713, 0.5958, 0.8127
t = 14: 0.8410, 0.6496, 0.8866
t = 15: 0.9119, 0.7044, 0.9616
t = 16: 0.9845, 0.7605, 1.0386
t = 17: 1.0578, 0.8172, 1.1163
t = 18: 1.1325, 0.8750, 1.1957
t = 19: 1.2094, 0.9344, 1.2771
t = 20: 1.2880, 0.9953, 1.3606
t = 21: 1.3680, 1.0571, 1.4453
t = 22: 1.4498, 1.1205, 1.5321
t = 23: 1.5341, 1.1858, 1.6216
t = 24: 1.6206, 1.2526, 1.7131
t = 25: 1.7094, 1.3214, 1.8072
t = 26: 1.7998, 1.3913, 1.9030
t = 27: 1.8927, 1.4633, 2.0014
t = 28: 1.9879, 1.5370, 2.1022
t = 29: 2.0854, 1.6126, 2.2056
t = 30: 2.1853, 1.6900, 2.3114
t = 31: 2.2881, 1.7696, 2.4202
t = 32: 2.3939, 1.8515, 2.5321
t = 33: 2.5021, 1.9354, 2.6467
t = 34: 2.6133, 2.0215, 2.7642
t = 35: 2.7280, 2.1106, 2.8857
t = 36: 2.8455, 2.2017, 3.0101
t = 37: 2.9668, 2.2957, 3.1386
t = 38: 3.0921, 2.3929, 3.2712
t = 39: 3.2204, 2.4922, 3.4067
t = 40: 3.3523, 2.5946, 3.5464
t = 41: 3.4888, 2.7006, 3.6911
t = 42: 3.6292, 2.8097, 3.8398
t = 43: 3.7741, 2.9222, 3.9931
t = 44: 3.9247, 3.0394, 4.1527
t = 45: 4.0793, 3.1597, 4.3168
t = 46: 4.2393, 3.2843, 4.4866
t = 47: 4.4053, 3.4142, 4.6636
t = 48: 4.5760, 3.5480, 4.8461
t = 49: 4.7541, 3.6886, 5.0383
t = 50: 4.9407, 3.8364, 5.2390

G. Structure Preservation Qualitative Comparison

We compare how changing color with our intervention method impacts image structure to that of changing the prompt to include the color. We see that our method much closer preserves the overall structure than color injection via prompt.



Figure 12. Comparison of the structural changes in images when comparing our color intervention to those by prompt-injected color.

Table 4. Comparison to other color-control alternatives.

Color Inj.	PRECISE (NATURAL, SMALL)			
	ΔE_{00} (\downarrow)	ΔH (\downarrow)	ΔS (\downarrow)	ΔL (\downarrow)
None	47	88	53	19
Prompt	31	52	31	13
Best of $N = 10_{None}$	40	86	53	16
Best of $N = 20_{None}$	36	84	52	14
Best of $N = 50_{None}$	34	82	53	13
Best of $N = 10_{Prompt}$	24	46	31	10
Best of $N = 20_{Prompt}$	23	48	30	9
Best of $N = 50_{Prompt}$	21	46	30	9
Color Peel (Butt et al., 2024)	31	68	32	12
<i>ReNO</i> _{SDXL} (Eyring et al., 2024)	28	58	33	11
<i>ReNO</i> _{FLUX} (Eyring et al., 2024)	27	34	27	12
Ours local	14	30	16	5
Ours global	16	34	15	8

Precise color control is a challenging task which cannot be solved easily training free. Specifically, most existing methods require high compute, either in the form of training or at inference time. This makes it impossible to scale generation to the 4,080 images used in the natural setting in the main paper (20 objects, 51 colors, 4 seeds). Instead, we use a subset including the 15 most basic colors (Red, Orange, Yellow, Chartreuse, Green, Spring Green, Cyan, Azure, Blue, Violet, Magenta, Rose, Black, White, Gray), the same 20 objects, and 1 seed for a total of 300 tested images.

The first additional comparison method is *best of N*, in which N images are generated, and the image with the lowest ΔE_{00} among them is selected. This results in N times the inference cost, which can become extreme for high N . We include versions of this baseline applied to both our *None* (prompt given without color) and *Prompt* (color specified in prompt), and test $N = 10, 20, 50$.

The next comparison method is *ColorPeel* (Butt et al., 2024), a training-based method that requires optimizing parameters for each target color. Therefore, computational costs scale by the number of unique colors required, unlike our intervention method which does not incur additional costs for new colors.

Finally, we compare with *ReNO* (Eyring et al., 2024), which can be used for more accurate prompt following. ReNO leverages test-time noise optimization to maximize prompt-following, therefore incurring per-image optimization cost.

Despite incurring less cost than any of these methods, our intervention achieves more precise color match in terms of ΔE_{00} , ΔH , ΔS , and ΔL . It is also the only method among these that leverages insights of inner model workings to improve the capabilities of the base model, rather than adding more uninterpretable optimization.

Table 5. Our intervention method’s performance on high (bright) and low (muted) saturation colors.

Color Inj.	PRECISE (NATURAL, BRIGHT)				PRECISE (NATURAL, MUTED)			
	ΔE_{00} (\downarrow)	ΔH (\downarrow)	ΔS (\downarrow)	ΔL (\downarrow)	ΔE_{00} (\downarrow)	ΔH (\downarrow)	ΔS (\downarrow)	ΔL (\downarrow)
None	45	90	57	14	33	90	22	14
Prompt	31	38	35	10	19	40	18	9
Ours local	16	14	15	5	16	22	14	7
Ours global	19	12	11	9	21	24	18	12

Table 6. Our intervention method’s performance on high (light) and low (dark) lightness colors.

Color Inj.	PRECISE (NATURAL, LIGHT)				PRECISE (NATURAL, DARK)			
	ΔE_{00} (\downarrow)	ΔH (\downarrow)	ΔS (\downarrow)	ΔL (\downarrow)	ΔE_{00} (\downarrow)	ΔH (\downarrow)	ΔS (\downarrow)	ΔL (\downarrow)
None	45	90	57	37	32	90	57	15
Prompt	25	38	38	25	22	30	37	7
Ours local	17	22	45	13	19	22	42	8
Ours global	20	24	42	16	24	24	32	10

We break down our main results into sub-categories, to develop a fine-grained understanding of our color intervention method’s performance under different settings in Tables 5 and 6. *Bright* and *Muted* refer to high and low saturation colors, and *Light* and *Dark* refer to high and low lightness.